



TEXAS TECH UNIVERSITY  
Libraries™

**ELECTRON EMISSION FROM METAL EMITTERS SUBJECT TO A HIGH  
INTENSITY LASER IN THE PRESENCE OF DC ELECTRIC FIELDS**

The Texas Tech community has made this publication openly available. [Please share](#) how this access benefits you. Your story matters to us.

Citation	D. Guo, S. N. Sami, and R. P. Joshi, "Electron emission from metal emitters subject to a high intensity laser in the presence of DC electric fields," <i>AIP Advances</i> <b>9</b> , 105302 (2019). <a href="https://doi.org/10.1063/1.5122212">https://doi.org/10.1063/1.5122212</a>
Citable Link	<a href="https://hdl.handle.net/2346/86902">https://hdl.handle.net/2346/86902</a>
Terms of Use	<a href="#">CC BY 4.0</a>

# Electron emission from metal emitters subject to a high intensity laser in the presence of DC electric fields

Cite as: AIP Advances **9**, 105302 (2019); <https://doi.org/10.1063/1.5122212>

Submitted: 29 July 2019 . Accepted: 25 September 2019 . Published Online: 08 October 2019

D. Guo, S. N. Sami, and  R. P. Joshi

## COLLECTIONS

Paper published as part of the special topic on [Chemical Physics](#), [Energy, Fluids and Plasmas](#), [Materials Science](#) and [Mathematical Physics](#)



View Online



Export Citation



CrossMark

## ARTICLES YOU MAY BE INTERESTED IN

[Enhanced efficiency in 808 nm GaAs laser power converters via gradient doping](#)

AIP Advances **9**, 105206 (2019); <https://doi.org/10.1063/1.5109133>

[Influences of experimental parameters on characteristics of focusing through scattering media by wavefront shaping](#)

AIP Advances **9**, 105014 (2019); <https://doi.org/10.1063/1.5098363>

[Holographic scanning confocal microscopy for both reflected light and fluorescence light imaging](#)

Review of Scientific Instruments **90**, 106103 (2019); <https://doi.org/10.1063/1.5116244>



# Electron emission from metal emitters subject to a high intensity laser in the presence of DC electric fields

Cite as: AIP Advances 9, 105302 (2019); doi: 10.1063/1.5122212

Submitted: 29 July 2019 • Accepted: 25 September 2019 •

Published Online: 8 October 2019



View Online



Export Citation



CrossMark

D. Guo, S. N. Sami, and R. P. Joshi<sup>a)</sup> 

## AFFILIATIONS

Department of Electrical and Computer Engineering, Texas Tech University, Lubbock, Texas 79409, USA

<sup>a)</sup>Corresponding author: Email: [ravi.joshi@ttu.edu](mailto:ravi.joshi@ttu.edu)

## ABSTRACT

Electron emission driven by both a strong DC applied bias and a superimposed laser field is examined through numerical simulations. Heating at the electrode surface that creates a dynamic, nonequilibrium electron distribution is included based on appropriate rate-equation analyses for energy balance. Much higher emission currents are predicted that follow the AC oscillations over the femtosecond range. The hot carrier population are predicted to persist much longer to yield a more gradual decay in the emission current beyond laser termination. The numerical results are also extended to an emitter array, given the interest in such configurations for obtaining high output coherent currents. The capability can subsequently be extended to assess the coherence and emittance of the electron source based on Monte Carlo transport techniques.

© 2019 Author(s). All article content, except where otherwise noted, is licensed under a Creative Commons Attribution (CC BY) license (<http://creativecommons.org/licenses/by/4.0/>). <https://doi.org/10.1063/1.5122212>

## I. INTRODUCTION

Ultrafast, laser-driven electron emission from metal nanostructures is of interest for free electron lasers and as sources of electrons in high power microwave devices. Applications range from photoelectron injectors for accelerators and free electron lasers,<sup>1</sup> and even has relevance to time-resolved imaging of fundamental processes in solid state physics,<sup>2,3</sup> chemistry,<sup>4</sup> and biology.<sup>5</sup> Applying strong electric fields to a metallic tip with nanometer sharpness enables electron emission via tunneling, producing continuous electron beams with high brightness and coherence.<sup>6,7</sup> Furthermore, illumination of such tips by femtosecond laser pulses, in combination with a moderate dc voltage applied to the tip, has realized pulsed field emission with femtosecond and nanometer resolution. This has opened up avenues for both basic research and new applications like time-resolved electron microscopy, spectroscopy, holography, and free-electron lasers.<sup>8</sup> Photoemission from lasers with small pulse-widths affords tightly bunched bursts having low emittance.

As such, the physics of photoemission has been well studied for both weak and strong laser fields.<sup>9–11</sup> Here, while electron emission driven by both a strong DC applied bias and a strong laser field

is examined, as was done previously by Zhang and Lau,<sup>12</sup> the role of heating by the laser to create dynamic, nonequilibrium electron distributions is additionally incorporated. Field screening in multi-emitter arrays is also discussed. The theory is first developed, and results presented for the emission current as a function of time, at different DC fields and AC intensities. The role of electron heating on the photoemission is also probed. While the emission currents are predicted to follow the AC oscillations over the femtosecond range, the hot carrier population persists much longer to yield a more gradual decay in the emission current. The numerical results are then extended to an emitter array, since the latter configurations are of interest from the standpoint of obtaining high current outputs. As might be expected, the role of screening and decreases in electric field due to proximity between adjacent emitters arise, and are treated and discussed here on the basis of equivalent charge models.

## II. MODEL DETAILS

### A. Time dependent transmission coefficient

The time-dependent transmission coefficient can be obtained from a solution of the time-dependent Schrodinger wave equation.

A solution to this problem involving both DC and AC electric fields was reported by Truscott<sup>13</sup> and Wagner<sup>14</sup> based on a co-ordinate transformation. More recently, an analysis for the transmission coefficient was discussed by Zhang and Lau<sup>12</sup> that included multiphoton processes, and both the optical and DC fields. Hence, only an outline of the inherent formulation is included here.

Outside the metal, the wavefunction  $\psi(z, t)$  is given by:

$$\begin{aligned} \psi(z, t) = & T_0 G_0(z, t) \exp(-i\omega t) \exp[i(k_x x + k_y y)] \\ & \times \exp[i\{qz F_1 \sin(\omega t)\}/(\hbar\omega) \\ & - iq^2 F_0 F_1 \sin(\omega t)\}/(\hbar m \omega^3) \\ & + iq^2 F_1^2 \sin(2\omega t)\}/(8\hbar m \omega^3)], \quad z \geq 0 \end{aligned} \quad (1)$$

where  $T_0$  is the transmission coefficient, and  $G_0$  given by the following expression:

$$G_0 = Ai(-\eta_0) - i Bi(-\eta_0). \quad (2)$$

In eqn. (1) above,  $F_0$  and  $F_1$  are the magnitudes of the DC and AC fields,  $\omega$  the angular frequency of the optical excitation,  $\hbar$  the reduced Planck's constant,  $m$  the electron effective mass,  $z$  the coordinate normal to the metal-air interface, and  $t$  the time. In addition,  $\eta_0 = \{E_0/(q F_0) + \xi\} (2qmF_0/\hbar^2)^{1/3}$ , with  $E_0 = E - E_F - W - U_p$ ,  $\xi = z + \{q F_1/(m \omega^2)\} \cos(\omega t)$ , and  $U_p = q^2 F_1^2/(4m \omega^2)$ . In the above, the work-function is denoted by  $W$ , while  $E_F$  represents the Fermi energy. Finally in Eqn. (1),  $k_x$ , and  $k_y$  denote wavevectors in the transverse direction.

Inside the metal, the wavefunction is given by:

$$\begin{aligned} \psi(z, t) = & \exp(-i\omega t) \exp[i(k_x x + k_y y + k_z z)] \\ & + R_0 \exp(-i\omega t) \exp[i(k_x x + k_y y + k_z z)]. \end{aligned} \quad (3)$$

where  $R_0$  is the reflection coefficient. Continuity of the wavefunction and its derivative at the interface ( $z=0$ ), then yields solutions for  $T_0$  and  $R_0$ . The ratio  $R(k_z, t)$  of the transmitted current density to the incident current density ( $= J_{tran}/J_{inc}$ ), can be obtained after some algebra. Some of the steps are outlined in [Appendix](#), and the final expression is:

$$R(k_z, t) = |T_0|^2 [k_e/(\pi k_z) + (p(t)/k_z) \{ (Ai)^2 + (Bi)^2 \}], \quad (4)$$

where  $p(t) \equiv \frac{q F_1 \sin(\omega t)}{\hbar \omega}$ . The emission current density,  $J_{tran}$ , transmitted from the metal can then be obtained as given below:

$$J_{tran} = \int \int \int q v_z R(k_z) [1/(2\pi)^3] 2k_{||} dk_{||} d\theta dk_z f(k_{||}, k_z), \quad (5)$$

once the distribution function  $f(k_{||}, k_z)$  for the electrons inside the metal is known.

## B. Electron distribution function with heating

The electron distribution function needed for the current density calculation was computed in a dynamic fashion, based on rate equations that embody energy exchanges between the electron and phonon sub-systems. In the process, energy gain by the electrons from the incident optical radiation, which deposits energy onto the metal, is taken into account. This is offset by energy losses from the electron sub-system through electron-phonon interactions which represent relaxation processes. A single lumped electron-phonon coupling constant has been assumed. Furthermore, for simplicity,

the decay of phonons via the anharmonic phonon-phonon coupling has been modeled on the basis of an effective phonon lifetime  $\Gamma_{ph}$ . The coupled rate equations provide a time-dependent lattice temperature  $T_e(t)$ , involving the following rate equations:

$$p_{abs} - G[T_e(t) - T_L(t)] = C_e dT_e(t)/dt, \quad (6a)$$

and

$$G[T_e(t) - T_L(t)] = C_L [dT_L(t)/dt + \{T_L(t) - T_0\}/\Gamma_{ph}], \quad (6b)$$

where  $G$  is the electron-phonon coupling constant (taken to be  $4 \times 10^{16}$  W/m<sup>3</sup>/K as a typical value for gold), while  $C_e$  and  $C_L$  are the electronic and lattice heat capacities. These values, based on the literature<sup>15</sup> have been taken here to be:  $C_e = 71.5$  J/m<sup>3</sup>/K<sup>2</sup>  $T_e$ , with  $\Gamma_{ph} = 7$  ps and  $C_L = 3.5 \times 10^6$  J/m<sup>3</sup>/K. Also,  $T_e(t)$  and  $T_L(t)$  are the effective temperatures of the electrons and the host lattice,  $t$  denotes the time, and  $P_{abs}$  is the power density (in Watts/m<sup>3</sup>). Finally,  $T_0$  denotes the ambient lattice temperature, while  $\Gamma_{ph}$  is the phonon lifetime of 7 ps due to anharmonic decay.<sup>16,17</sup> The input power was related to the field strength  $F_1$  of incident optical signal. The coupled set of equations (6) were solved using the fourth-order Runge-Kutta method.

For the electron system, the distribution function  $f_e(t)$  was taken to comprise of two parts given by:<sup>18</sup>

$$f_e(T_e, t) = f_{e-N T}(t) + f_{e-T}(T_e, t), \quad (7)$$

where  $f_{e-N T}(t)$  and  $f_{e-T}(t)$  denote the non-thermal and thermal components. The thermal part of the electron distribution was taken to be the usual Fermi-Dirac, but at an elevated, time-dependent temperature  $T_e(t)$ . The non-thermal part of the distribution  $f_{e-N T}(t)$ , was obtained at each time  $t$  and energy  $E$  based on the following relation:

$$\begin{aligned} f_{e-N T}(E, t + dt) = & f_{e-N T}(E, t) - f_{e-N T}(E, t) \{ [E - E_f]/E_f \}^2 dt/\Gamma_0 \\ & + [p_{abs} dt/(\hbar\omega)] [(E - \hbar\omega)/E]^{1/2} T \\ & / \{ \exp[(E - \hbar\omega - E_f)/(kT_e(t))] + 1 \}. \end{aligned} \quad (8)$$

where,  $T = \frac{1}{\int_{E_F - \hbar\omega}^{E_F} \frac{\sqrt{E}}{1 + \exp \frac{E - E_f}{kT_e(t)}} dE}$ .

In the above equation, the first term on the right side of the equation (8) represents the current state, while the second term takes account of the loss in occupancy over an elemental time step  $dt$  due to the electron-electron interactions. The last term arises from photon absorption. It was derived based on the assumption of a smooth density of states with a  $\sim E^{1/2}$   $dE$  dependence over an incremental energy range  $dE$ .

## III. RESULTS AND DISCUSSION

The time-dependent evolution of the electron temperature obtained in response to an incident power input from a constant laser source is shown in [Figure 1a](#). The energy density was taken to be  $2 \times 10^{13}$  W/m<sup>2</sup>. A sharp rise to about  $2 \times 10^4$  °K is predicted within about 1.5 ps, followed by a more gentle rise. This heating of the electrons affects the overall distribution. As might be expected, the temperature reaches a saturating value at a point in time when the losses from the electron subsystem begin to equal the energy gain from the input laser. However, in practice, such a laser cannot be sustained for long periods, and so a finite duration laser pulse presents

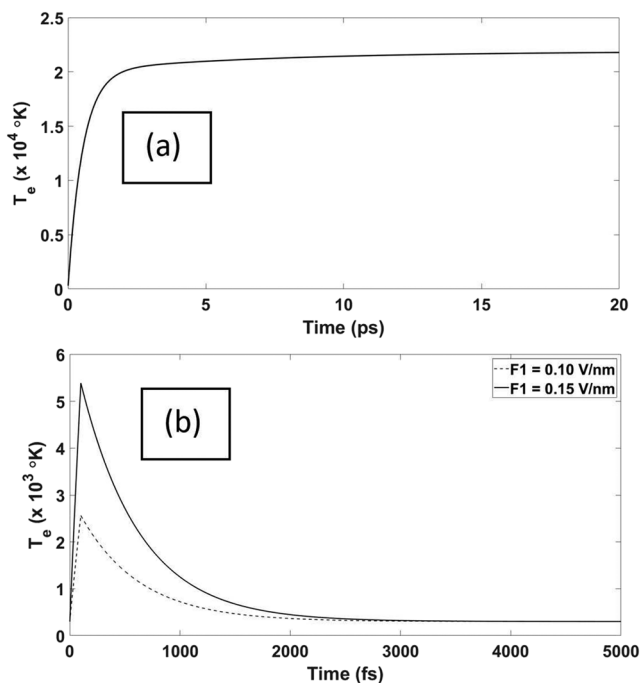


**FIG. 1.** Effective electron temperatures as a function of time following two different incident laser excitation waveforms on a gold electrode. (a) Response to a unit step function, and (b) a 100 fs laser excitation.

a more reasonable waveform. Taking a 100 fs pulse, the temperature evolution  $T_e(t)$  was obtained for two different AC field intensities ( $F_I$ ) of 0.1 V/nm and 0.15 V/nm, respectively. The results are given in Figure 1(b). The peak electron temperatures of 2563 °K and 5391 °K for the two AC field strengths are predicted at the end of the 100 fs pulse.

Based on the above time-dependent electron temperature  $T_e(t)$  formulation, the combined distribution  $f_e(T_e, t)$  comprised of both the thermal and nonthermal components was obtained for  $F_I = 10^8$  V/m. This value is quite large, but does help demonstrate the nonequilibrium changes and disparities in the distribution function. Later, smaller and more reasonable values of  $F_I$  have been chosen. The distribution at four different time instants of 50 fs, 100 fs, 200 fs, and 500 fs are shown in Figure 2. The Fermi level was at 5.53 eV and is marked on the figure. Due to the heated, nonequilibrium, nonthermal contribution, the  $f_e(T_e, t)$  curve exhibits a relative “shoulder” at the 100 fs instant with elevated values at the higher energies. Beyond the 100 fs time, the distribution function is predicted to gradually fall and evolve towards its equilibrium state.

The emission current densities resulting from combined fields (i.e., both  $F_0$  and  $F_I$ ) can be expected to naturally exhibit undulations because of the superimposed AC component in the driving excitation. The values over a few cycles, as obtained from the calculations, are shown in Figure 3 for  $F_0 = 7 \times 10^9$  V/m,  $F_I = 10^7$  V/m, and incident laser power of  $1.33 \times 10^{11}$  W/m<sup>2</sup>. For clarity, the inset shows the behavior up to 40 fs. Upon termination of the laser pulse, the oscillations in the current density cease, and the values exhibit a

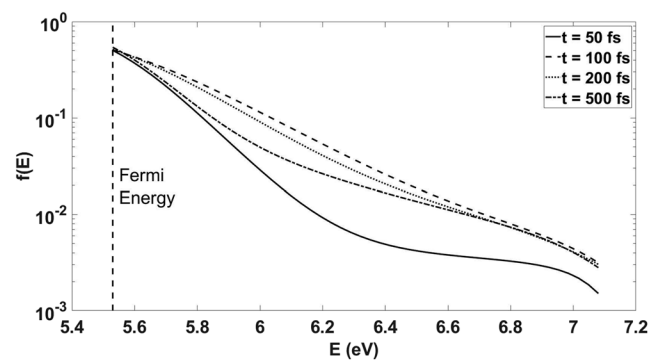


**FIG. 2.** Snapshots of the overall combined distribution function  $f_e(T_e, t)$  as a function of electron energy at four time instants of 50 fs, 100 fs, 200 fs, and 500 fs.

slow but gradual decrease over time. The latter, almost imperceptible over the time scales shown, is the result of the slow relaxation of the distribution function as the electron cool in the presence of ongoing interactions with the phonons. Upon taking the average over last cycle prior to laser termination, at different DC biasing levels, the field dependent behavior shown in Figure 4 for the current density ( $J_{tran}$ ) emerged. For comparison, values of  $J_{tran}$  for the equilibrium Fowler-Nordheim (F-N) case are also shown in the figure. The two consequences apparent in the curves of Figure 4 are: (i) higher predicted currents for the non-equilibrium case as compared to the F-N levels because of the highly energetic distribution function which reduces transmission probabilities for a larger fraction of the electrons, and (ii) reduced threshold fields for the start of non-negligible currents.

Finally, the above modifications to the emission current density were probed for the case of multiple emitters in an array. For such analysis it is crucial to first determine the electric fields in the vicinity of the emitting tips. As is well known, the presence of multiple emitters in close proximity to each other leads to a screening effect with reductions in the peak electric field magnitudes.<sup>19</sup> As shown in the recent past, such effects can conveniently and simply be probed

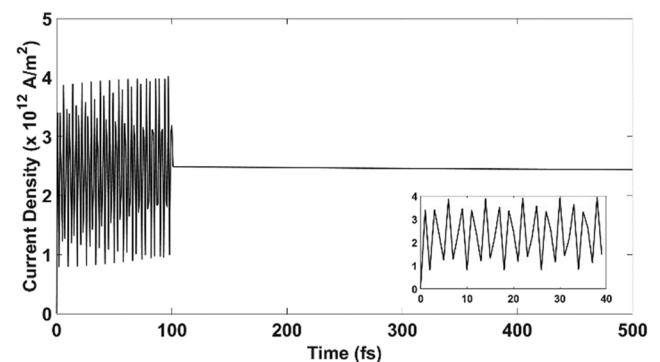


**FIG. 3.** Simulation results of the time-dependent electron emission current density in response to a 100 fs laser pulse with inclusion of electron temperature increases and evolution of a nonequilibrium distribution function.

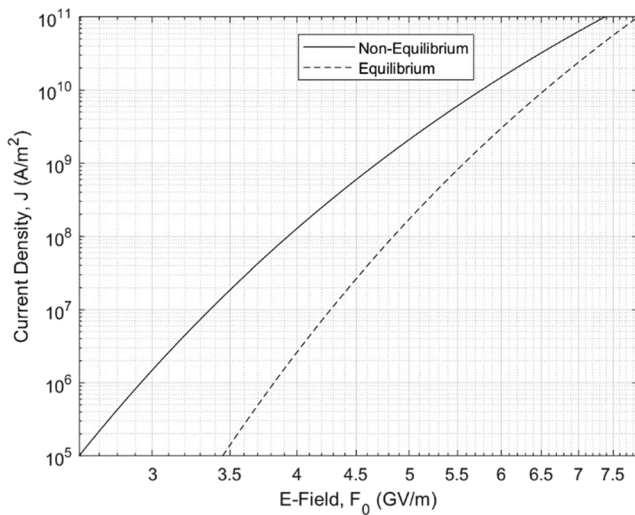


**FIG. 4.** Emitted electron current density as a function of electric field, based on assumptions of equilibrium and nonequilibrium electron distribution functions.

on the basis of Line Charge Models (LCMs) which approximate the surface of an ungated, large aspect ratio field emitter tip by appropriate equipotentials above a dipole line charge.<sup>20</sup> The advantage of the LCM, and similar models,<sup>21–23</sup> is that they facilitate the study of key array parameters, such as emitter height, tip radius, and array geometry, while invoking conceptual simplicity. These models yield quick solutions to the potentials and electric field distributions for a nanoemitter array, and are designed to provide an equivalent structure consisting of a line charge and its image, to replace the actual nanoprotusion. Simple analytic expressions are then made available as a result, instead of having to solve a three-dimensional problem with the affiliated boundary conditions.

However, as pointed out recently by Biswas et al.,<sup>23</sup> the LCM generically mimics ellipsoidal emitters rather than a Cylindrical-Post-with-an-Ellipsoidal-Tip (CPET) that is typical of nanowires. An ellipsoidal emitter would be governed by the following equation in cylindrical co-ordinates:  $z^2/z_1^2 + r^2/(a_1 z_1) = 1$ , with the radius of curvature at the tip of the major axis (the emitter tip, essentially) equal to  $a_1$ . Charge densities beyond the linear regime, for example a quadratic charge distribution, would allow for modeling shapes that are closer to a CPET. Here, in order to address such aspects, higher-order charge density distributions from multiple rings were used in determining the electric fields and the screening effects in multi-emitter arrays. For example, the equipotential contours were improved in going from a three-ring to a nine-ring model, as shown in Fig. 5. For these calculations of Fig. 5, emitters of 1500  $\mu\text{m}$  height and tip radius of 47.43  $\mu\text{m}$  were used to ensure a high aspect ratio. The distribution of charges for the two cases is listed in Table I. The use of multiple rings can be seen to improve the potential profiles. For example, the slight undulation near the emitter surface at a height of  $\sim 1400$   $\mu\text{m}$  in Fig. 5(a) is smoothed out in Fig. 5(b). In the present scheme, a charged ring was first set up close to the tip. Next, numerous other charge rings were added sequentially at different locations to ensure that the resulting equipotential

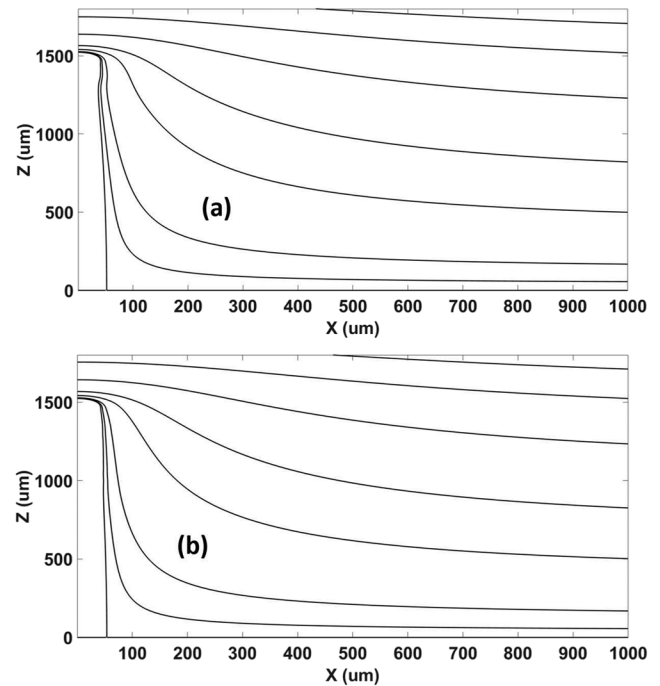


**FIG. 5.** Equipotential profiles near a single emitter of 1500  $\mu\text{m}$  height and tip radius of 47.43  $\mu\text{m}$  based on a linear charge model (LCM) with: (a) three charged rings, and (b) nine charged rings.

contour from the emitter top to its base remained straight. Thus, the placement of an additional  $N^{\text{th}}$  ring was governed by the need to smooth out the occurrence of any undulation in the potential profile from the collective effect of the  $N-1$  rings and their images, over any region.

The nine-ring model was applied to multi-emitter arrays to probe screening in arrays. The predicted electric field values at the

**TABLE I.** Details of the three and nine-ring models of the 1500  $\mu\text{m}$  high nanoemitter.

Height ( $\mu\text{m}$ )	Ring radius ( $\mu\text{m}$ )	Charge ( $10^{-10}$ C)
3 – Ring Model		
1490	4.018	2.721505
1420	12.5	4.09219
1371	5.6	3.49624
9 – Ring Model		
1490	4.018	2.7215
1420	12.5	4.09219
1371	5	3.49624
1324	5.5	2.62218
1259	10	2.18515
1200	13	1.370685
1140	13	1.092575
1082	30	0.655545
1000	25	0.53635

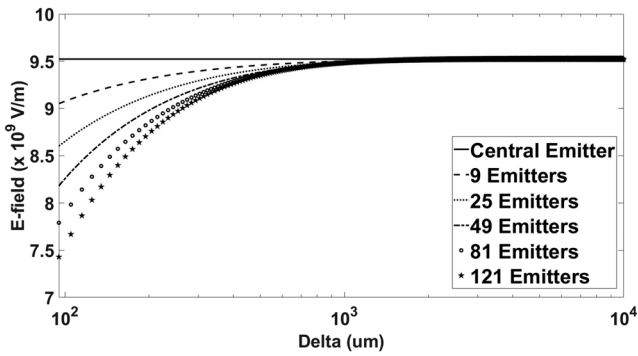


**FIG. 6.** Predicted electric field values at the emitter tip as a function of emitter spacing ( $\delta$ ) for various numbers of emitters in the array.

emitter tip as a function of emitter spacing ( $\delta$ ) for various numbers of emitters in an array are shown in Fig. 6. The peak field is predicted to reduce down to about 79% of the value for an isolated emitter at a 100  $\mu\text{m}$  separation. Furthermore, the screening effect is predicted to almost disappear when separations equal the emitter height.

#### IV. SUMMARIZING CONCLUSIONS

Thus, electron emission driven by both a strong DC applied bias and a superimposed laser field has been examined, with inclusion of the heating that can create dynamic, nonequilibrium electron distributions. The evolution of the electron temperatures and the energy distribution was obtained on the basis of dynamic rate equations to ensure energy balance. While the emission currents are predicted to follow the AC oscillations over the femtosecond range, the hot carrier population persists much longer to yield a more gradual decay in the emission current beyond termination of the laser. Much higher emission currents were predicted due to the heating produced by the photoexcitation. The numerical results were then extended to an emitter array, given the interest in such configurations for obtaining high output coherent currents. The treating based on local charge models, naturally included the role of screening and proximity effects.

In actual practice, the electron emission from the metal would depend on details of the internal scattering governed by both electron-electron, electron-phonon, and electron-plasmon interactions. This would fashion the characteristics, such as the energies, velocities, angular directions etc. of the emergent electron swarm. These aspects would be important for assessing the coherence and emittance of the electron source. The details could be treated by

Monte Carlo transport techniques,<sup>24,25</sup> and will be the focus of subsequent analysis.

#### ACKNOWLEDGMENTS

Useful discussion with Profs. Lau (UM) and Zhang (MSU) are gratefully acknowledged. This work was supported in part by grants from the Office of Naval Research (N00014-18-1-2382), and the Air Force Office of Scientific Research (FA9550-19-1-0056).

#### APPENDIX: TRANSMITTED CURRENT RATIO

Inside the metal, the wavefunction is given by:

$$\psi(z, t) = \exp(-i\omega t) \exp[i(k_x x + k_y y + k_z z)] + R_0 \exp(-i\omega t) \exp[i(k_x x + k_y y - k_z z)], \quad z \leq 0 \quad (\text{A1})$$

where  $R_0$  is the reflection coefficient,  $k_x, k_y, k_z$  are the wavevectors along the  $x$ -,  $y$ - and  $z$ -directions,  $\omega$  is the angular frequency, and  $t$  the time. Here, the  $z=0$  defines the interface. On the transmitted side, the wavefunction  $\psi(z, t)$  is given by:

$$\psi(z, t) = T_0 G_0(z, t) \exp(-i\omega t) \exp[i(k_x x + k_y y + k_z z)] \times \exp[i\{qz F_1 \sin(\omega t)\}/(\hbar\omega) - iq^2 F_0 F_1 \sin(\omega t)/(\hbar m \omega^3) + iq^2 F_1^2 \sin(2\omega t)/(8\hbar m \omega^3)], \quad z > 0 \quad (\text{A2})$$

where  $T_0$  is the transmission coefficient. Matching wavefunctions at  $z = 0$  leads to:

$$1 + R_0 = T_0 G_0(0, t) \exp[-iA(t)], \quad (\text{A3})$$

where

$$A(t) \equiv q^2 F_0 F_1 \sin(\omega t)/(\hbar m \omega^3) - q^2 F_1^2 \sin(2\omega t)/(8\hbar m \omega^3), \quad (\text{A4})$$

$$G_0 = Ai(-\eta_0) - iBi(-\eta_0), \quad (\text{A5})$$

$$\eta_0 = \{E_0/(qF_0) + \xi\}k_e, \quad \text{with } E_0 = E - E_F - W - Up, \quad (\text{A6})$$

$$\xi = z + \{qF_1/(m\omega^2)\}\cos(\omega t), \quad \text{and } Up = q^2 F_1^2/(4m\omega^2), \quad (\text{A7})$$

and

$$k_e = (2qmF_0/\hbar^2)^{1/3}. \quad (\text{A8})$$

Matching the derivatives of the wavefunctions at  $z = 0$  yields:

$$ik_z - ik_z R_0 = T_0 \frac{\partial G_0(z, t)}{\partial z} \exp[-iA(t)] + T_0 G_0(0, t) \times \exp[-iA(t)] \frac{i\{qF_1 \sin(\omega t)\}}{\hbar\omega}. \quad (\text{A9})$$

Finally, using  $\frac{\partial G_0}{\partial z} = -k_e(Ai' - iBi')$ , some algebra leads to:

$$|T_0|^2 = \frac{4}{\left[ \left\{ Ai \left( 1 + \frac{\{qF_1 \sin(\omega t)\}}{\hbar\omega k_e} \right) + \frac{k_e}{k_z} Bi' \right\}^2 + \left\{ \frac{k_e}{k_z} Ai' - Bi - \frac{\{qF_1 \sin(\omega t)\}}{\hbar\omega k_e} Bi \right\}^2 \right]}. \quad (\text{A10})$$

The incident current density  $J_{inc}$  is given by:

$$J_{inc} = \frac{i\hbar}{2m} (-2ik_z) = \frac{\hbar k_z}{m}, \quad (\text{A11a})$$

while the transmitted current density  $J_{trans}$  given by:

$$J_{Trans} = \frac{i\hbar}{2m} \left( \psi \frac{\partial \psi^*}{\partial z} - \psi^* \frac{\partial \psi}{\partial z} \right). \quad (\text{A11b})$$

The transmitted current density then works out to:

$$J_{Trans} = \frac{\hbar |T_0|^2}{m} \left[ \frac{k_e}{\pi} + P \{ (Ai)^2 + (Bi)^2 \} \right], \quad (\text{A12})$$

where  $P \equiv \frac{qF_1 \sin(\omega t)}{\hbar\omega}$ .

So finally, the ratio  $R(k_z, t)$  of the transmitted current density to the incident current density ( $= J_{trans}/J_{inc}$ ) is obtained as:

$$R(k_z, t) = \frac{J_{Trans}}{J_{inc}} = |T_0|^2 \left[ \frac{k_e}{\pi k_z} + \frac{P(t)}{k_z} \{ (Ai)^2 + (Bi)^2 \} \right]. \quad (\text{A13})$$

## REFERENCES

- <sup>1</sup>V. Ayvazyan, N. Baboi, I. Bohnet, and R. Brinkmann, *Phys. Rev. Lett.* **88**, 104802 (2002).
- <sup>2</sup>M. Merano, S. Sonderegger, A. Crottini, S. Collin *et al.*, *Nature (London)* **438**, 479 (2005).
- <sup>3</sup>B. J. Siwick, J. R. Dwyer, R. E. Jordan, and R. J. D. Miller, *Science* **302**, 1382 (2003).
- <sup>4</sup>H. Ihee, V. A. Lobastov, U. M. Gomez, B. M. Goodson, R. Srinivasan, C. Y. Ruan, and A. H. Zewail, *Science* **291**, 458 (2001).
- <sup>5</sup>V. A. Lobastov, R. Srinivasan, and A. H. Zewail, *Proc. Natl. Acad. Sci. U.S.A.* **102**, 7069 (2005).
- <sup>6</sup>G. Furse, *Field Emission in Vacuum Microelectronics* (Kluwer Academic/Plenum Publishers, New York, 2003).
- <sup>7</sup>B. Cho, T. Ichimura, R. Shimizu, and C. Oshima, *Phys. Rev. Lett.* **92**, 246103 (2004).
- <sup>8</sup>H. Yanagisawa, C. Hafner, P. Doná, and M. Klöckner, *Phys. Rev. B* **81**, 115429 (2010).
- <sup>9</sup>P. Hommelhoff, C. Kealhofer, and M. A. Kasevich, *Phys. Rev. Lett.* **97**, 247402 (2006).
- <sup>10</sup>R. Bormann, M. Gulde, A. Weismann, S. V. Yalunin, and C. Ropers, *Phys. Rev. Lett.* **105**, 147601 (2010).
- <sup>11</sup>M. Pant and L. K. Ang, *Phys. Rev. B* **88**, 195434 (2013).
- <sup>12</sup>P. Zhang and Y. Y. Lau, *Scientific Reports* **6**, 19894 (2016).
- <sup>13</sup>W. S. Truscott, *Phys. Rev. Lett.* **70**, 1900 (1993).
- <sup>14</sup>M. Wagner, *Phys. Rev. Lett.* **76**, 4010 (1996).
- <sup>15</sup>W. S. Fann, R. Storz, H. W. K. Tom, and J. Bokor, *Phys. Rev. Lett.* **68**, 2834 (1992).
- <sup>16</sup>A. Majzoobi, R. P. Joshi, A. A. Neuber, and J. C. Dickens, *AIP Advances* **5**, 127237 (2015).
- <sup>17</sup>R. P. Joshi and D. K. Ferry, *Phys. Rev. B* **39**, 1180 (1989).
- <sup>18</sup>W. S. Fann, R. Storz, H. W. K. Tom, and J. Bokor, *Phys. Rev. B* **46**, 13592 (1992).
- <sup>19</sup>J. R. Harris, K. L. Jensen, J. J. Petillo, S. Maestas, W. Tang, and D. A. Shiffler, *Journ. Appl. Phys.* **121**, 203303 (2017).
- <sup>20</sup>J. R. Harris, K. L. Jensen, D. A. Shiffler, and J. J. Petillo, *Appl. Phys. Lett.* **106**, 201603 (2015).
- <sup>21</sup>E. M. Vinogradova, E. N. Egorov, and D. S. Televnyy, *Vacuum* **127**, 45 (2016).
- <sup>22</sup>E. Mesa, E. Dubado-Fuentes, and J. J. Saenz, *J. Appl. Phys.* **79**, 39 (1996).
- <sup>23</sup>D. Biswas, G. Singh, and R. Kumar, *J. Appl. Phys.* **120**, 124307 (2016).
- <sup>24</sup>For example, R. P. Joshi, S. Viswanatham, P. Shah, and R. del Rosario, *J. Appl. Phys.* **93**, 4836 (2003).
- <sup>25</sup>J. Roupie, O. Jbara, T. Tondou, M. Belhaj, and J. Puech, *Journal of Physics D* **46**, 125306 (2013).